

Emergence of broken-symmetry states at half-integer band fillings in twisted bilayer graphene

Saisab Bhowmik,^{1,*} Bhaskar Ghawri,² Nicolas Leconte,³ Samudrala Appalakondaiah,³
Mrityunjay Pandey,⁴ Phanibhusan S. Mahapatra,² Dongkyu Lee,^{3,5} K.
Watanabe,⁶ T. Taniguchi,⁷ Jeil Jung,^{3,5,†} Arindam Ghosh,^{2,4} and U. Chandni^{1,‡}

¹*Department of Instrumentation and Applied Physics,
Indian Institute of Science, Bangalore, 560012, India*

²*Department of Physics, Indian Institute of Science, Bangalore, 560012, India*

³*Department of Physics, University of Seoul, Seoul 02504, Korea*

⁴*Centre for Nano Science and Engineering, Indian Institute of Science, Bangalore 560 012, India*

⁵*Department of Smart Cities, University of Seoul, Seoul 02504, Korea*

⁶*Research Center for Functional Materials, National Institute for
Materials Science, Namiki 1-1, Tsukuba, Ibaraki 305-0044, Japan*

⁷*International Center for Materials Nanoarchitectonics,
National Institute for Materials Science, Namiki 1-1, Tsukuba, Ibaraki 305-0044, Japan*

The dominance of Coulomb interactions over kinetic energy of electrons in narrow, non-trivial moiré bands of magic-angle twisted bilayer graphene (TBG) gives rise to a variety of correlated phases such as correlated insulators [1–3], superconductivity [2, 4–7], orbital ferromagnetism [2, 8, 9], Chern insulators [10–13] and nematicity [14]. Most of these phases occur at or near an integer number of carriers per moiré unit cell. Experimental demonstration of ordered states at fractional moiré band-fillings at zero applied magnetic field B , is a challenging pursuit. In this letter, we report the observation of states near half-integer band-fillings of $\nu \approx 0.5$ and ± 3.5 at $B \approx 0$ in TBG proximitized by tungsten diselenide (WSe₂) through magnetotransport and thermoelectricity measurements. A series of Lifshitz transitions due to the changes in the topology of the Fermi surface implies the evolution of van Hove singularities (VHSs) of the diverging density of states (DOS) at a discrete set of partial fillings of flat bands. Furthermore, at a band filling of $\nu \approx -0.5$, a symmetry-broken Chern insulator emerges at high B , compatible with the band structure calculations within a translational symmetry-broken supercell with twice the area of the original TBG moiré cell. Our results are consistent with a spin/charge density wave ground state in TBG in the zero B -field limit.

In two-dimensional electron systems, a quantizing magnetic field B is an essential ingredient for the experimental realization of both integer and fractional quantum Hall states. The first proposal for a zero- B analogue of the integer quantum Hall effect (QHE) came from the Haldane model [15], where non-interacting electrons hopping on a honeycomb lattice with a zero-average, spatially inhomogeneous B exhibit quantized Hall conductances. Subsequently, interacting lattice models with nearly flat Chern bands proposed fractional QHE in the absence of B [16, 17]. The key to realizing

these fractional states is the search for materials with extremely flat bands featuring non-trivial topological properties. TBG, where two graphene sheets are stacked together with a rotational mismatch near the first magic-angle of 1.1° , is an ideal material platform to investigate such zero- B states. Recent experiments have revealed a plethora of broken-symmetry phases in TBG [1, 2, 4, 5, 8–14, 18, 19] and related moiré materials [20–23], where the external tuning of several parameters leads to the desired symmetry breaking. For instance, C_2 inversion symmetry can be broken by aligning the TBG layers with hexagonal Boron Nitride (hBN) [9], while the application of a B -field breaks time reversal symmetry T . These experimental knobs enable access to the low energy degrees of freedom of the band structure, which hosts non-trivial topological, as well as trivial band insulators at or near integer fillings of the moiré unit cell. Incompressible states stabilized by electron-electron interactions within the flat band, were found to appear at large B -fields, in the form of Hall plateaus featuring Chern numbers C at various band filling index s [10–13, 24]. Recently, transport measurements in TBG uncovered a high B -field-induced state at $s = 3.5$, suggesting the possibility of a new VHS and fractional Chern insulator [11]. However, states originating from fractional fillings of the unit cell at zero or weak B -field have remained elusive in TBG devices, although a recent report on twisted monolayer-bilayer graphene indicates incompressible insulators with $C = 1$ at fractional band fillings of $s = 1.5$ and 3.5 [20]. Notably, states at several fractional fillings have been observed in transition metal dichalcogenide (TMD)-based moiré systems, attributed to generalized Wigner crystallization of the underlying lattice and charge density waves ordering [25]. States featuring fractional C and/or fractional s , which unify the possibility of many exotic states such as spin/charge density wave phases (fractional s), symmetry broken Chern insulators (integer C , fractional s), and fractional Chern insulators (fractional C and s), are thus of great interest to our growing understanding of this fascinating material platform. While all these states emerge from strong electron-electron interactions within the flat

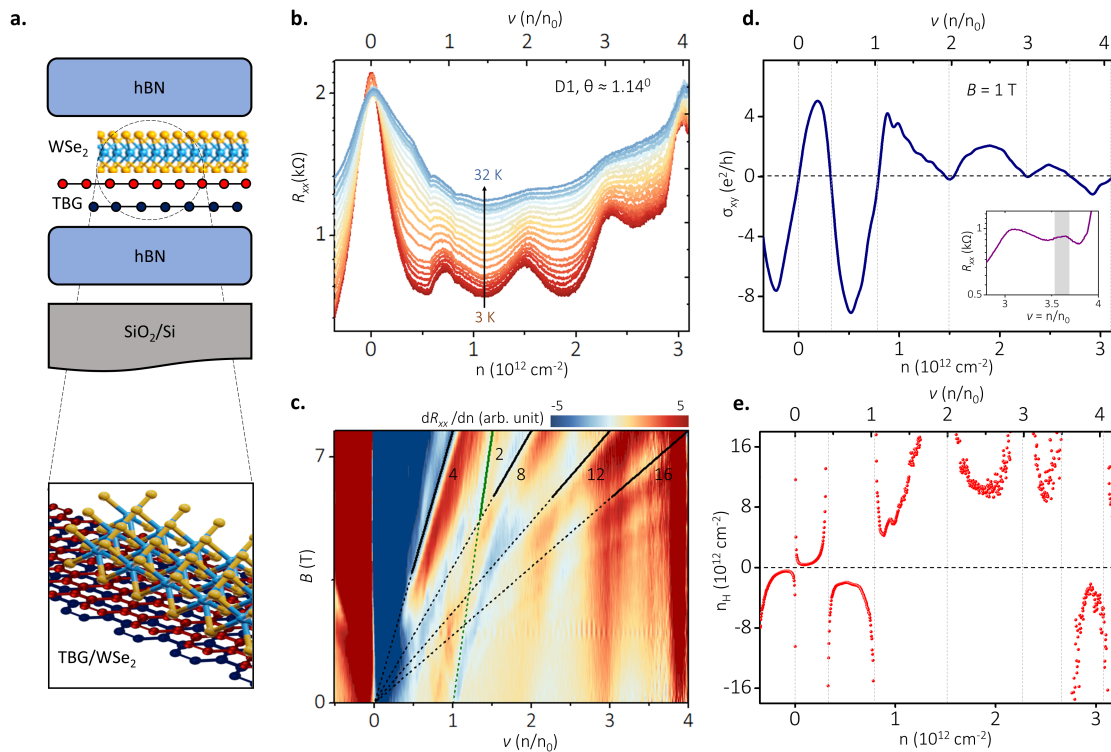


FIG. 1. **Electrical characterization and low-field Hall measurements in device D1, $\theta \approx 1.14^\circ$.** **a.** Schematic of hBN encapsulated TBG/WSe₂ heterostructure on SiO₂/Si substrate. **b.** Four-probe longitudinal resistance R_{xx} as a function of carrier density n measured in the temperature T range 3–32 K for $B = 0$. The twist angle $\theta \approx 1.14^\circ$ was calculated from the position of the resistance peak at a filling ν (n/n_0) = 4 where n_0 is the density corresponding to one carrier per moiré unit cell. **c.** Landau fan diagram at $T = 5$ K for magnetic field B up to 7.75 T where dR_{xx}/dn is plotted as a function of (ν, B) . The Landau levels (LL) diverging from the charge neutrality point (CNP) are shown by solid black lines. The filling factors 4, 8, 12, and 16 are determined from the slopes of these lines. In addition, a straight line with a slope of 2 that nucleates from $\nu = 1$ at $B \gtrsim 5$ T is shown by the solid green line. **d.** Density dependence of field-symmetrized Hall conductivity σ_{xy} at $B = 1$ T and $T = 6$ K. Zero-crossings appear at $\nu = 0, 0.5, 1, 3.5$ and 4. σ_{xy} suddenly drops to zero at $\nu = 2$ and 3 and rises again upon crossing $\nu = 2$ and 3. The inset shows an additional peak in $R_{xx}(n)$ around $\nu = 3.5$, when $B = 0$. This data in R_{xx} was recorded after a magnetic field sweep and the peak at $\nu = 3.5$ persisted at zero-field for the next few thermal cycles. **e.** Hall density n_H , calculated from Hall resistance R_{xx} exhibits similar behavior as σ_{xy} .

bands, subtle changes in experimental configurations can modify the anisotropy energy that decides the preferred ordered phase when the degenerate phases are in close competition [26, 27].

In this work, we report the observation of novel states at half-integer moiré band fillings in TBG/WSe₂ devices, that persist at $B \approx 0$, suggesting the possibility of a spin/charge density wave order. We focus on magneto-transport and thermoelectric transport measurements on two TBG/WSe₂ moiré heterostructures D1 and D2, with twist angles $\theta \approx 1.14^\circ$ and 1.16° respectively, fabricated using the ‘tear and stack’ technique (see Methods and Supplementary Fig. S6) [4, 28]. Few-layer WSe₂ flake of thickness ≈ 2 -3 nm was placed on the TBG, sandwiched between two hBN layers, with the stack assembled on SiO₂/Si substrate (Fig. 1a). Characterization for D1 starts in Fig. 1b with the four-probe longitudinal resistance R_{xx} as a function of charge carrier density (n) in

the temperature (T) range of 3–32 K for $B = 0$ T. The hole side in device D1 was inaccessible due to dielectric leakage. We observe correlated states at all partial fillings $\nu = 1, 2$, and 3 and a resistive peak at $\nu = 4$, where the conduction band is fully occupied. The twist angle ($\theta \approx 1.14^\circ$) is estimated from the density at the superlattice gap ($\nu = 4$) (see Methods). The resistance at $\nu = 1, 2, 3$ increases with increasing temperature in the measured range, and the peaks disappear at higher T . Further, we observe that linear-in- T behavior of $R_{xx}(n)$ at $\nu = 1, 2$ and 3 persists up to $T = 32$ K (see Supplementary Fig. S8). Device D2 also exhibits similar correlated states at different ν across various contact configurations (see Supplementary Fig. S7). Fig. 1c shows the Landau fan diagram for device D1 in a perpendicular B -field, where the linearly dispersing features emanating from the charge neutrality point (CNP) and other band fillings can be characterized by fitting the Diophantine equation, $n/n_0 = C\phi/\phi_0 + s$, where n_0 is the density

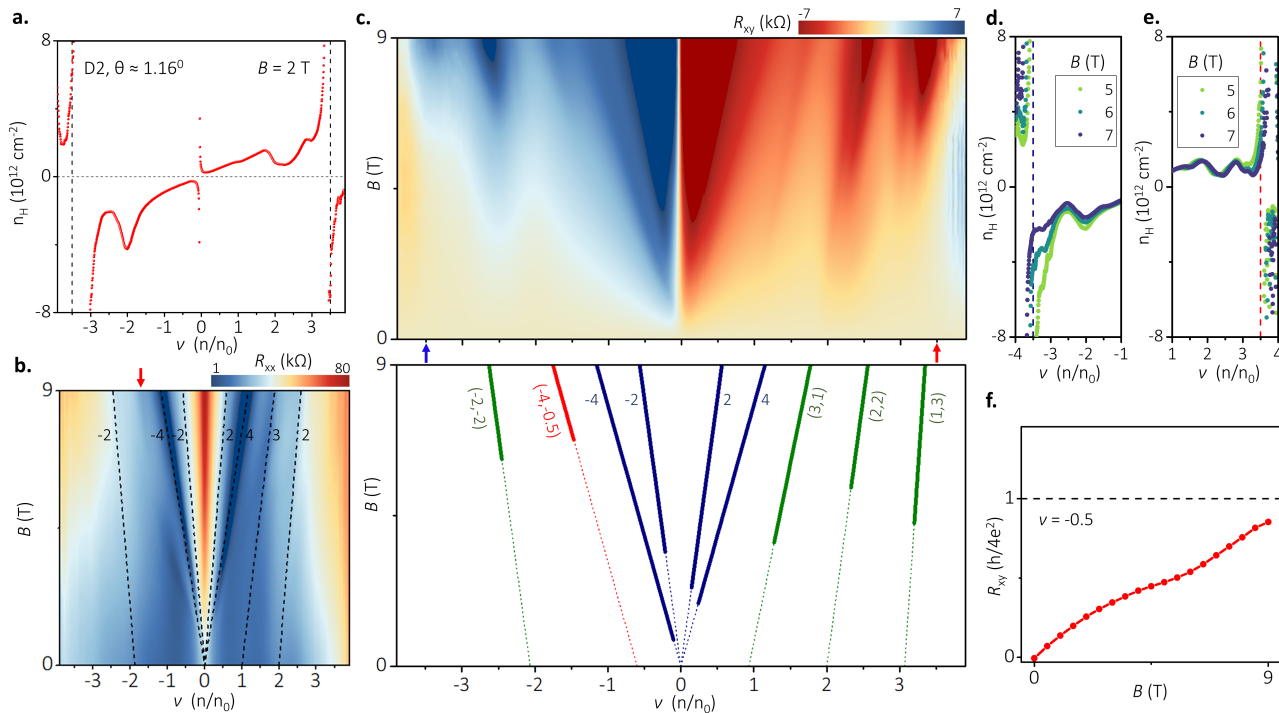


FIG. 2. **Symmetry-broken states at $\nu \approx -0.5$ and ± 3.5 in device D2, $\theta \approx 1.16^\circ$.** **a.** n_H vs. ν at $B = 2$ T and $T = 5$ K shows sign-changes at $\nu = 0, \pm 3.5$ and reset at $\nu = \pm 2$. **b.** R_{xx} as a function of ν for different B up to 9 T and the color bar shown here is in logarithmic scale. The minima in R_{xx} emanating from $\nu = 0$ have slopes of $\pm 2, \pm 4$, while those from $\nu = 1$ and ± 2 have slopes 3 and ± 2 , respectively. An additional state develops at $B \gtrsim 6.5$ T whose position in density at $B = 9$ T is marked by the red arrow on the top axis. **c.** R_{xy} vs (ν, B) at $T = 5$ K shows multiple states at different ν . The red and blue arrows in the bottom axis mark $\nu = +3.5$ and $\nu = -3.5$ respectively, where R_{xy} changes sign. In the bottom panel, these states are labelled by $(C, \nu) = (\pm 4, 0), (\pm 2, 0)$ (solid blue), $(1, 3), (\pm 2, 2), (3, 1)$ (solid green) and $(-4, -0.5)$ (solid red). **d-e.** n_H exhibits sign changes at $\nu = \mp 3.5$ for high magnetic fields (5-7 T). **f.** R_{xy} at $\nu \approx -0.5$ for different B , along the red line in the lower panel in (c) that approaches the quantized limit $R_{xy} = h/4e^2$ as the field is increased.

corresponding to one carrier per moiré unit cell, ϕ is the magnetic flux per moiré unit cell, $\phi_0 = h/e$ is the flux-quantum, h is Planck's constant, e is the charge of electron, and s is the band filling index or the number of carriers per unit cell at $B = 0$ T. The slope gives the Chern number via the Streda formula, $C (= h/e \partial n / \partial B)$. The Landau-levels (LLs) diverging from the CNP have filling factors of 4, 8, 12, and 16 (black lines) that increase in steps of 4 due to the four-fold spin/valley degeneracy. For $B \gtrsim 5$ T, we observe an additional state that can be extrapolated to $\nu = 1$ at $B = 0$, with a slope of 2 (green line). We now focus on the low B -field Hall measurements. Fig. 1d shows Hall conductivity $\sigma_{xy}(n, B)$ as a function of n at a perpendicular $B = 1$ T. We find that, while zero-crossings of σ_{xy} are observed, as expected, at the CNP and the band insulator at $\nu = 4$, a 'reset' behaviour is observed at $\nu = 2, 3$, namely σ_{xy} decreases to zero and rises again through $\nu = 2$ and 3 without any sign change. These features have been reported in earlier studies of TBG and related systems [11, 29], and have been attributed to enhanced Coulomb interactions within the malleable bands that favor a gap opening by splitting the band into a low-energy filled and high-energy empty sub-band when the Fermi energy E_F crosses the VHS at $\nu = 2$. A similar

splitting of the bands that occur at the consequently developed VHS at $\nu = 3$, leads to yet another reset [11]. Surprisingly, some novel observations with respect to earlier work are the additional zero-crossings in $\sigma_{xy}(n)$ at $\nu = 1$ and half-integer $\nu = 0.5$ and 3.5. Intriguingly, a minor peak in $R_{xx}(n)$ around $\nu = 3.5$ was seen even at $B = 0$ in several later thermal cycles as shown in the inset to Fig. 1d. It is often illustrative to plot the Hall density n_H , calculated from Hall resistance R_{xy} as $n_H = -\frac{1}{e} \frac{B}{R_{xy}}$, which provides insights into the VHSs and Fermi surface topology. In Fig. 1e, n_H exhibits features consistent with σ_{xy} , diverging with opposite signs on both low and high-density sides of $\nu = 0.5, 1$ and 3.5. Furthermore, no sign-reversal in n_H is observed at $\nu = 2, 3$. Remarkably, we find robust states at half-integer ν even at B -fields as low as ~ 0.3 T in device D1 (see Supplementary Fig. S9).

To further investigate the presence and robustness of states at fractional fillings we report in Fig. 2 detailed magnetotransport measurements in a second device D2. We observe similarities and differences, the latter possibly due to specific device details. Consistent with device D1, sign changes are observed in n_H at $\nu = \pm 3.5$, down to $B = 0.2$ T (see Fig. 2a for $B = 2$ T and

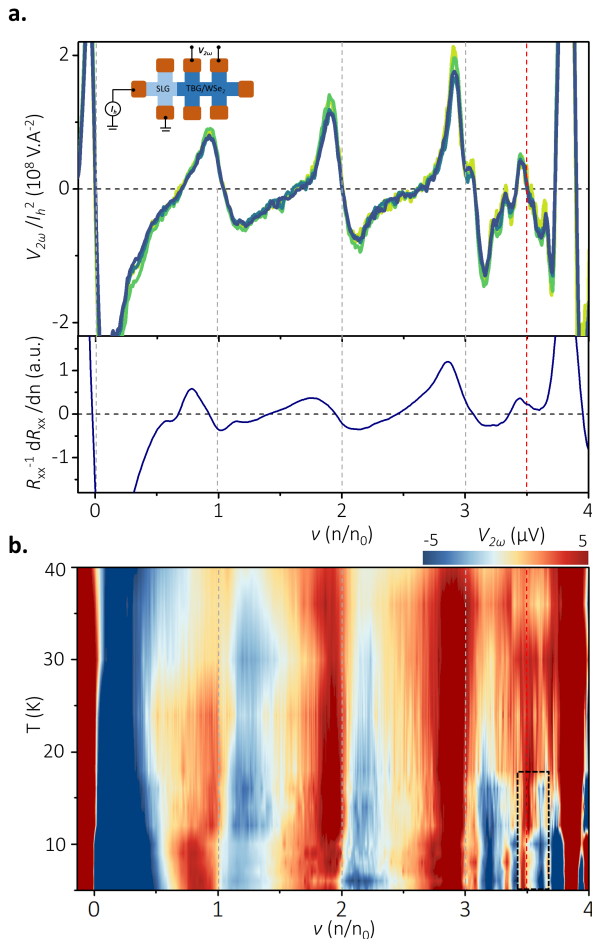


FIG. 3. Density-dependence of zero-field thermoelectricity. **a.** Second harmonic component of thermo-voltage $V_{2\omega}$ as a function of n for heating currents $I_h = 300 - 400$ nA, with a step size of 20 nA, measured at $T = 5$ K. A schematic of the heating geometry and measurement of $V_{2\omega}$ can be found in the inset. For all I_h , the values of $V_{2\omega}/I_h^2$ are constant, which indicates the linear response regime in the range of I_h used for heating. Sign-reversals at $\nu = 1, 2, 3$ are marked by vertical dotted lines (grey). An additional zero-crossing appears at $\nu = 3.5$ (red dotted line). $(1/R_{xx})dR_{xx}/dn$ is shown in the bottom panel. Both $V_{2\omega}$ and R_{xx} are measured independently in the same thermal cycle. **c.** Temperature dependence of $V_{2\omega}$ in the range 5 – 40 K. We observe a series of sign changes as n is swept across the different correlated phases. Two vertical regions with opposite signs in $V_{2\omega}$ on the low and high density sides of $\nu = 3.5$ are outlined by a rectangular window for clarity. The zero-crossing at $\nu = 3.5$ disappears around $T \gtrsim 18$ K.

supplementary Fig. S10), which remain robust at high B as well (Fig. 2d-e). Further, n_H shows reset of charge carriers at $|\nu| = 2$ similar to device D1. Fig. 2b and 2c show the Landau fan diagrams in R_{xx} and R_{xy} respectively. The filling factors of ± 2 emanating from the CNP indicate that the four-fold spin/valley symmetry is broken. Additionally, multiple linearly dispersing minima in R_{xx} are observed at high B , originating from various s . We also note that these minima in R_{xx} are

accompanied by the wedge-like resistive features in R_{xy} (Fig. 2c). Our observation of possible Chern insulators, labelled by the two indices C and integer s with $(C, s) = (\pm 2, \pm 2), (1, 3)$ and $(3, 1)$ are in a good agreement with recent reports on TBG systems [10–13]. Chern insulators at integer s can be understood within the two spin/valley degenerate flat band model in TBG where C_2T symmetry breaking opens a gap at the CNP and produces isolated flat Chern bands with opposite Chern numbers $C = +1$ and $C = -1$ [10–13, 30]. The most striking feature in our data is a new state at half-integer $s \approx -0.5$ for $B \gtrsim 6.5$ T (denoted by red arrow in Fig. 2b and red line in the lower panel of Fig. 2c) for which we obtain $C = -4$ from Streda formula in both R_{xx} and R_{xy} . The magnetic field evolution of the state along the same red line in Fig. 2c is shown in Fig. 2f, where we observe that R_{xy} approaches $h/4e^2$ within the experimental range of B -field, providing further evidence for the Chern insulating state.

While Hall measurements demonstrate the existence of states at fractional fillings for low B , the technique precludes direct observation of these states at $B = 0$. With this aim, we have performed thermoelectric transport measurements at $B = 0$ for device D1. The experimental technique used for measurement of the thermo-voltage is briefly discussed below and in methods section. A temperature gradient (ΔT) over the entire TBG/WSe₂ channel is created by passing a sinusoidal current (I_h) through SLG contacts outside the twisted region, shown in the inset of Fig. 3a. We measure the second-harmonic component of thermo-voltage $V_{2\omega}$ for different I_h (described in detail elsewhere [31]) in a density range from the CNP to $\nu = 4$ (Fig. 3a). The linear variation of $V_{2\omega}$ with I_h^2 ensures a linear response regime for the range of heating currents used. The n -dependence of $V_{2\omega}$ shows a series of zero-crossings at $\nu = 0, 1, 2, 3$. Most importantly, we observe that the sign-reversal of $V_{2\omega}$ also occurs at half-integer $\nu = 3.5$ at $B = 0$. In Fermionic systems at very low temperatures ($T \ll T_F$, where T_F is the Fermi temperature), where scattering of charge carriers is diffusive, semiclassical Mott relation (SMR) establishes a connection between thermoelectric power ($S = V_{2\omega}/\Delta T$) and electrical resistance (R_{xx}) [31, 32] as,

$$S_{\text{Mott}} = \frac{\pi^2 k_B^2 T}{3|e|} \frac{1}{R_{xx}} \frac{dR_{xx}}{dn} \frac{dn}{dE} \Big|_{E_F}, \quad (1)$$

where $\frac{dn}{dE}$ represents the DOS. In deriving the SMR, a non-interacting scenario is assumed with the electrical conductance varying smoothly near E_F . SMR holds true in a large number of van der Waals materials, including monolayer and bilayer graphene [33, 34] and disordered metals/insulators. We compare $V_{2\omega}$ with derivative of R_{xx} with respect to n , shown in the bottom panel of Fig. 3a. We observe exact mapping of zero-crossings at $\nu = 1, 2$ and 3, with peaks in R_{xx} . While, $\frac{dR_{xx}}{dn}$ shows a weak peak at $\nu = 3.5$, a clear sign change is observed in $V_{2\omega}$. Intriguingly, the state at $\nu = 0.5$ does not appear at $B = 0$ in either R_{xx} or $V_{2\omega}$. This we believe is because the

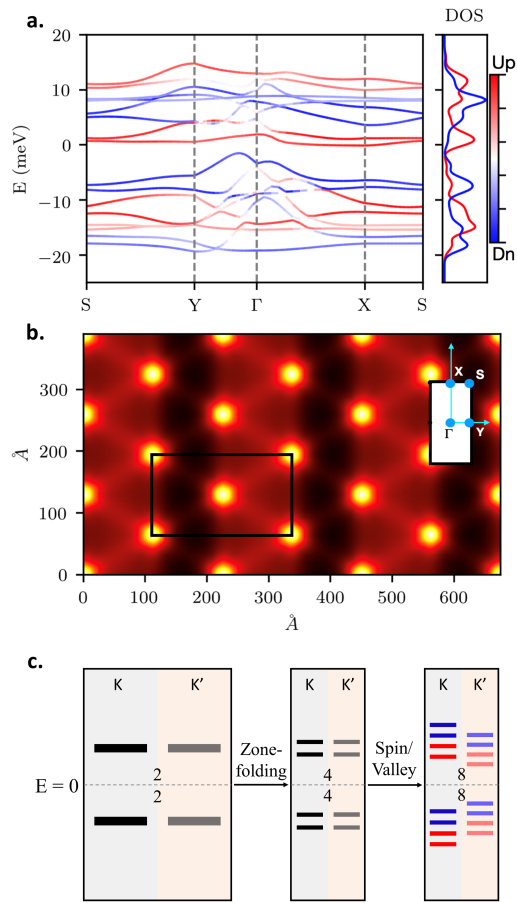


FIG. 4. **Degeneracy lifting of the folded bands.** **a.** Spin-resolved band structure and corresponding DOS of TBG under a 1D periodic potential given in Eq. 2 with $C_0 = 0$, $C_z = 30$ meV, $\phi = 0$, $\Delta = 300$ meV, $t_2 = 15$ meV and $\lambda_R = 10.5$ meV. The red and blue shades indicate the strength of the respective spin orientations induced by the SOC terms. **b.** Schematic that combines the colormap of the interlayer distances from the relaxed TBG system (AA stackings appear as bright dots) together with the 1D sine potential whose zero is at AA-stacking to illustrate the rectangular cell whose area is twice as large as that of TBG moiré unit cell. The inset represents the high symmetry points and the k -path corresponding to the band structure in the main panel. **c.** The sketch illustrates how the zone-folding doubles the number of flat bands and halves the Brillouin zone area, while splitting of the spin and valley degrees of freedom bring the total number of bands to 16. The high/low intensity of colors for the lines distinguish the K and K' valleys and the red and blue colors refer to the spin degree of freedom. The valley-degeneracy lifting is illustrated by a small shift in the K' valley levels with respect to the bands in the K valley.

sign changes in $V_{2\omega}$ occur in accordance with the resistive peaks in R_{xx} , while the sign changes in σ_{xy} and n_H are intricately connected to the Fermi surface topology via R_{xy} . The temperature dependence of $V_{2\omega}$ is illustrated in Fig. 3b. The sign reversals are seen as a series of vertical red and blue bands throughout the measured T range. While the transitions at the CNP and $\nu = 1, 2$

are robust and persist up to the measured temperature of $T = 40$ K, the feature at $\nu = 3.5$ vanishes for $T \gtrsim 18$ K.

The emergence of distinct features in magnetotransport and thermoelectricity at half-integer band fillings for two different devices, despite the inevitable variability typically seen in TBG samples, suggest a robust mechanism behind our observations. We speculate that strong correlations between electrons may generate a spin/charge density order that breaks translation symmetry in the moiré leading to Brillouin zone (BZ) folding with electron wave functions extending over a unit cell with doubled area. In the non-interacting, single-particle band structure of TBG, a VHS is expected to appear at $|\nu| = 2$, which is the half-filling of the first low-energy non-dispersive conduction or valence band, separating a two-pocket Fermi surface around the K -points from a higher-energy single-pocket Fermi surface around the Γ -point of the moiré BZ. This has been consistently verified in transport experiments [4, 11, 35]. Broken translational symmetry and appearance of folded BZ in the doubled moiré unit cell may favor VHS at $\nu = 1$ and other partial fillings instead, as observed in our devices. While higher order translational symmetry breaking (tripling, quadrupling) is a possibility, we can not rule out the presence of an inherent, accidental VHS at $\nu = 0.5$ in the TBG/WSe₂ band structure either. As noted in the theoretical model below, additional spin splitting of bands can lead to a complex DOS hierarchy, which can explain the VHS features at half integer fillings. Furthermore, the emergence of a Chern insulator at $\nu \approx -0.5$ in device D2, strengthens the possibility of a doubled moiré unit cell. We also remark that the observation of a state with a slope of $C = 2$ as obtained from Streda formula from a band filling of $s = 1$ for device D1, is reminiscent of an odd parity ($p = C + s$) Chern insulator, recently reported in compressibility measurements of TBG due to reconstruction of Chern bands driven by the modulation of charge density waves over the real space moiré unit cell [36].

In the following we illustrate in Fig. 4a the band structure of TBG subject to a 1D density wave potential that doubles the moiré unit cell area (Fig. 4b) and hence the number of bands, similar to the proposal in twisted monolayer-bilayer graphene [20]. The four-fold degenerate conduction and valence bands would turn into two eight-fold degenerate bands upon zone-folding when the supercell area is doubled. In Fig. 4c, we schematically illustrate the degeneracy lifting of these bands resulting in a total of sixteen split bands in the presence of spin/charge density potential patterns. The states at half-integer fillings observed in experiments are therefore compatible with an odd integer filling of the zone-folded split bands. Our proposal of 1D patterned phases whose periods are commensurate with the moiré patterns can give rise to fractionally filled flat bands, analogous to the Bloch band filling index $s = \pm 1/3, 1/2$ states seen in Landau levels [37] that can be justified in the presence of Wigner crystal phases [38]. Our tight-binding Hamilto-

nian in the carbon π -orbitals basis incorporates this 1D pattern through a sinusoidal function and further incorporates the sublattice staggering as well as the intrinsic and Rashba spin-orbit coupling potentials that are often introduced when describing proximity spin-orbit coupling of graphene on transition metal dichalcogenide (TMD).

$$\begin{aligned}
H = & \sum_{l,m,\sigma} t_{lm} c_{l\sigma}^\dagger c_{m\sigma} + \sum_{l,\sigma} (C_0 + \xi_l C_z) \sin\left(\frac{\pi x_l}{\lambda_{\text{TBG}}} + \phi\right) c_{l\sigma}^\dagger c_{l\sigma} \\
& + \sum_{l_t,\sigma} \xi_{l_t} \Delta c_{l_t\sigma}^\dagger c_{l_t\sigma} + \sum_{\langle\langle l_t, m_t \rangle\rangle\sigma} \nu_{l_t m_t} t_2 e^{i\pi/2} c_{l_t\sigma}^\dagger c_{m_t\sigma} \\
& + \frac{2i}{3} \sum_{\langle l_t, m_t \rangle} \sum_{\sigma, \sigma'} c_{l_t\sigma}^\dagger c_{m_t\sigma'} [\lambda_R (\hat{\mathbf{s}} \times \mathbf{d}_{l_t m_t})_z]_{\sigma\sigma'}.
\end{aligned} \tag{2}$$

Here, the first term describes the carbon interatomic hopping terms that are tuned to generate the magic angle flat bands at 1.08° [39], see the supplementary information for the expression of the distance-dependent t_{lm} terms. The l, m indices are lattice labels l_t, m_t with the t subscript referring to top layer sites that are contacting the TMD. The second 1D sine term describes a density wave potential repeating with a period of $2\lambda_M^{\text{TBG}}$, twice the TBG moiré period, which defines a supercell that doubles the moiré area and allows to obtain folded bands that split at half-integers of the unperturbed system's filling factors. The ϕ phase term is a control knob that shifts the potential origin position. The remaining three terms capture the WSe₂ interface effect in the contacting graphene layer through a constant mass term with unequal sublattice resolved potentials, and through Kane-Mele and Rashba SOC models, where $\nu_{l_t m_t} = \pm 1$ following the conventions in Ref. [17] where $\hat{\mathbf{s}}$ are the spin Pauli matrices and $\mathbf{d}_{l_t m_t}$ is the displacement vector between lattice sites l_t and m_t . These terms introduce an energy anisotropy that favors a certain spin/valley isospin polarization of the ground-state [40]. Because the lattice constant mismatch between TBG and WSe₂ is already large, the proximity spin-orbit coupling terms [41] in graphene do not change drastically when we modify the twist angle from alignment. The system parameters for the band structures are *ad hoc* choices that illustrate the degeneracy lifting of the folded flat bands compatible with the observed half-integer filling of $\nu = 0.5$ and 3.5 , and the gaps at the integer filling of $\nu = 2$ and 3 (partially). The simultaneous presence of mass with opposite $\xi_l = \pm 1$ signs for A, B sublattice resolved potentials and SOC terms can cause valley and spin splitting that lifts the degeneracy between the flat bands which the Coulomb interactions can further amplify. We refer to the supplementary information for the bands associated with alternative $\phi = \pi/2$ cosine-like 1D potential that illustrates the overall robustness to shifts in its origin.

Our work shows that generation of flat bands by means of moiré superlattices is enriched by the possibility of superposing periodic potentials that are commensurate

with the original moiré pattern [42]. The favored ground state among several quasi-degenerate phases will depend on the anisotropy energy for the different spin/valley isospin polarization that can change with details in sample preparation and device assembly methods. Here, we have only considered the $s = 1/2$ Bloch band filling index scenario, while $s = \pm 1/3$ for Kekule patterns with three times larger superlattice area seen in experiments with Graphene/hBN [37, 38] also deserve attention in future research. Different specific material choices for the TBG dielectric environment are expected to subtly influence the ground state configuration. In particular, the way in which the spin and valley isospins order for various fillings will impact system properties like the spin or orbital magnetism stemming from the topological nature of the bands, the superconducting pairing symmetry as well as the instabilities in the electron-electron and electron-hole channels. Our work suggests that using TMD dielectrics is a promising pathway to further understand and explore the nature of fractional-filling correlated states in the limit of vanishing magnetic fields. This prospect is ever brighter, thanks to the large variety of TMD materials that could be used to engineer moiré heterostructures.

Note added in proof: While preparing our manuscript, we became aware of related observations of fractional Chern insulators in hBN-interfaced magic-angle TBG reported in [43] at filling fractions different than in our work.

METHODS

Device fabrication

The devices in this work were fabricated using a modified ‘tear and stack’ method (see Supplementary Fig. S6). A hBN flake (10 – 22 nm) was picked up using a polypropylene carbonate (PPC) film that was coated on a polydimethylsiloxane (PDMS) stamp. The hBN flake was then used to pick up a multilayer WSe₂ ($\sim 2 - 3$ nm). Next, hBN/WSe₂ was slowly placed on a monolayer graphene flake. After picking up the first half of the graphene, torn by hBN, the transfer stage was rotated approximately by 1.1° , and the second half of the graphene was picked up. In the final step, a thick hBN flake (25 – 30 nm) was picked up, and the encapsulated stack was released on a 285 nm SiO₂/Si wafer at a temperature of 85°C . We set the temperature at 63°C for picking up hBN and 55°C for picking up graphene and WSe₂. The PPC film was then cleaned with anisole and organic solvents. We defined the Hall bar geometry of the final device using electron-beam lithography, reactive ion etching using CHF₃/O₂, and thermal evaporation of ohmic edge contacts using Cr/Au (5 nm/60 nm). WSe₂ crystals used in this work were obtained from 2D Semiconductors.

Transport Measurements

Electrical and thermoelectric transport measurements were carried out in a pumped Helium cryostat with 9 T magnetic field. Magnetotransport measurements were performed using a bias current of 10 – 100 nA using an SR830 low-frequency lock-in amplifier at 17.81 Hz. Local Joule heating was employed for thermoelectric measurements to create a temperature gradient across the TBG/WSe₂ region. A range of sinusoidal currents (300 – 400 nA) at an excitation frequency of $\omega = 17.81$ Hz was allowed to pass through the SLG region to create a temperature difference ΔT between two ends of the TBG/WSe₂ channel and the resulting 2nd harmonic thermo-voltage ($V_{2\omega}$) was recorded using the same lock-in amplifier. To estimate the twist angle, we used the relation, $n_s = 8\theta^2/\sqrt{3}a^2$ where $a = 0.246$ nm is the lattice constant of graphene and n_s ($\nu = 4$) is the charge carrier density corresponding to a fully filled superlattice unit cell.

Real-space lattice calculations

The atomic positions were relaxed using LAMMPS molecular dynamics simulations [44] based on EXX-RPA-informed [45] force-fields, and the electronic structure was obtained through real-space tight-binding calculations as outlined in the supplementary information. Both the band structure and DOS were calculated by a shift-invert diagonalization method [46] with a broadening of 0.8 meV, while the band structures in the absence of SOC terms are calculated using exact diagonalization. We used a 4x3x1 Monkhorst-Pack k-point grid for the DOS calculation in a rectangular supercell containing 22328 atoms. The graphene itself is modeled using the F2G2 model [47]. More details on the Hamiltonian implementation, analysis of the different terms in the Hamiltonian and phase shifted patterns can be found in the supplementary information.

ACKNOWLEDGEMENTS

We gratefully acknowledge the usage of the MNCF and NNFC facilities at CeNSE, IISc. UC acknowledges funding from SERB via grants ECR/2017/001566

and SPG/2020/000164. NL was supported by the Korean National Research Foundation grant NRF-2020R1A2C3009142 and AS by grant NRF-2020R1A5A1016518. DL was supported by the Korean Ministry of Land, Infrastructure and Transport(MOLIT) from the Innovative Talent Education Program for Smart Cities. JJ was supported by the Samsung Science and Technology Foundation under project SSTF-BAA1802-06. We acknowledge computational support from KISTI through grant KSC-2021-CRE-0389 and the resources of Urban Big data and AI Institute (UBAI) at the University of Seoul. KW and TT acknowledge support from the Elemental Strategy Initiative conducted by the MEXT, Japan (Grant Number JPMXP0112101001) and JSPS KAKENHI (Grant Numbers JP19H05790 and JP20H00354).

AUTHOR CONTRIBUTIONS

SB fabricated the device, performed the measurements, and analyzed the data. BG, MP, and PSM assisted in measurements/analysis. KW and TT grew the hBN crystals. AG and UC advised on experiments. NL, SA, DL, and JJ performed the theoretical calculations. SB, NL, JJ, and UC wrote the paper with inputs from other authors.

COMPETING INTERESTS

The authors declare no competing interests.

DATA AVAILABILITY

The data that support the findings of this study are available from the corresponding author upon reasonable request.

CODE AVAILABILITY

The code that support the findings of this study are available from the corresponding author upon reasonable request.

* saisabb@iisc.ac.in
 † jeiljung@uos.ac.kr
 ‡ chandniu@iisc.ac.in

- [1] Cao, Y. *et al.* Correlated insulator behaviour at half-filling in magic-angle graphene superlattices. *Nature* **556**, 80–84 (2018).
 [2] Lu, X. *et al.* Superconductors, orbital magnets and correlated states in magic-angle bilayer graphene. *Nature* **574**, 653–657 (2019).

- [3] Po, H. C., Zou, L., Vishwanath, A. & Senthil, T. Origin of Mott insulating behavior and superconductivity in twisted bilayer graphene. *Phys. Rev. X* **8**, 031089 (2018).
 [4] Cao, Y. *et al.* Unconventional superconductivity in magic-angle graphene superlattices. *Nature* **556**, 43–50 (2018).
 [5] Yankowitz, M. *et al.* Tuning superconductivity in twisted bilayer graphene. *Science* **363**, 1059–1064 (2019).
 [6] Wu, F., MacDonald, A. H. & Martin, I. Theory of phonon-mediated superconductivity in twisted bilayer

- graphene. *Phys. Rev. Lett.* **121**, 257001 (2018).
- [7] Lian, B., Wang, Z. & Bernevig, B. A. Twisted bilayer graphene: A phonon-driven superconductor. *Phys. Rev. Lett.* **122**, 257002 (2019).
- [8] Sharpe, A. L. *et al.* Emergent ferromagnetism near three-quarters filling in twisted bilayer graphene. *Science* **365**, 605–608 (2019).
- [9] Serlin, M. *et al.* Intrinsic quantized anomalous Hall effect in a moiré heterostructure. *Science* **367**, 900–903 (2020).
- [10] Nuckolls, K. P. *et al.* Strongly correlated Chern insulators in magic-angle twisted bilayer graphene. *Nature* **588**, 610–615 (2020).
- [11] Wu, S., Zhang, Z., Watanabe, K., Taniguchi, T. & Andrei, E. Y. Chern insulators, van Hove singularities and topological flat bands in magic-angle twisted bilayer graphene. *Nat. Mater.* **20**, 488–494 (2021).
- [12] Saito, Y. *et al.* Hofstadter subband ferromagnetism and symmetry-broken Chern insulators in twisted bilayer graphene. *Nat. Phys.* **17**, 478–481 (2021).
- [13] Das, I. *et al.* Symmetry-broken Chern insulators and Rashba-like Landau-level crossings in magic-angle bilayer graphene. *Nat. Phys.* **17**, 710–714 (2021).
- [14] Cao, Y. *et al.* Nematicity and competing orders in superconducting magic-angle graphene. *Science* **372**, 264–271 (2021).
- [15] Haldane, F. D. M. Model for a quantum hall effect without Landau levels: Condensed-matter realization of the “parity anomaly”. *Phys. Rev. Lett.* **61**, 2015–2018 (1988).
- [16] Sun, K., Gu, Z., Katsura, H. & Das Sarma, S. Nearly flatbands with nontrivial topology. *Phys. Rev. Lett.* **106**, 236803 (2011).
- [17] Neupert, T., Santos, L., Chamon, C. & Mudry, C. Fractional quantum hall states at zero magnetic field. *Phys. Rev. Lett.* **106**, 236804 (2011).
- [18] Stepanov, P. *et al.* Untying the insulating and superconducting orders in magic-angle graphene. *Nature* **583**, 375–378 (2020).
- [19] Zondiner, U. *et al.* Cascade of phase transitions and Dirac revivals in magic-angle graphene. *Nature* **582**, 203–208 (2020).
- [20] Polshyn, H. *et al.* Topological charge density waves at half-integer filling of a moiré superlattice (2021). arXiv:2104.01178 [cond-mat].
- [21] Hao, Z. *et al.* Electric field-tunable superconductivity in alternating-twist magic-angle trilayer graphene. *Science* **371**, 1133–1138 (2021).
- [22] Liu, X. *et al.* Tunable spin-polarized correlated states in twisted double bilayer graphene. *Nature* **583**, 221–225 (2020).
- [23] Rickhaus, P. *et al.* Density-wave states in twisted double-bilayer graphene (2020). arXiv:2005.05373 [cond-mat].
- [24] Song, Z. *et al.* All magic angles in twisted bilayer graphene are topological. *Phys. Rev. Lett.* **123**, 036401 (2019).
- [25] Xu, Y. *et al.* Correlated insulating states at fractional fillings of moiré superlattices. *Nature* **587**, 214–218 (2020).
- [26] Wilhelm, P., Lang, T. C. & Läuchli, A. M. Interplay of fractional Chern insulator and charge density wave phases in twisted bilayer graphene. *Phys. Rev. B* **103**, 125406 (2021).
- [27] Wolf, T. M. R., Lado, J. L., Blatter, G. & Zilberberg, O. Electrically tunable flat bands and magnetism in twisted bilayer graphene. *Phys. Rev. Lett.* **123**, 096802 (2019).
- [28] Kim, K. *et al.* van der waals heterostructures with high accuracy rotational alignment. *Nano Lett.* **16**, 1989–1995 (2016).
- [29] Saito, Y., Ge, J., Watanabe, K., Taniguchi, T. & Young, A. F. Independent superconductors and correlated insulators in twisted bilayer graphene. *Nature Physics* **16**, 926–930 (2020).
- [30] Po, H. C., Zou, L., Senthil, T. & Vishwanath, A. Faithful tight-binding models and fragile topology of magic-angle bilayer graphene. *Phys. Rev. B* **99**, 195455 (2019).
- [31] Ghawri, B. *et al.* Excess entropy and breakdown of semiclassical description of thermoelectricity in twisted bilayer graphene close to half filling (2020). arXiv:2004.12356 [cond-mat].
- [32] Jonson, M. & Mahan, G. D. Mott’s formula for the thermopower and the Wiedemann-Franz law. *Phys. Rev. B* **21**, 4223–4229 (1980).
- [33] Zuev, Y. M., Chang, W. & Kim, P. Thermoelectric and magnetothermoelectric transport measurements of graphene. *Phys. Rev. Lett.* **102**, 096807 (2009).
- [34] Jayaraman, A. *et al.* Evidence of lifshitz transition in the thermoelectric power of ultrahigh-mobility bilayer graphene. *Nano Letters* **21**, 1221–1227 (2021).
- [35] Kim, Y. *et al.* Charge inversion and topological phase transition at a twist angle induced van Hove singularity of bilayer graphene. *Nano Lett.* **16**, 5053–5059 (2016).
- [36] Pierce, A. T. *et al.* Unconventional sequence of correlated chern insulators in magic-angle twisted bilayer graphene (2021). arXiv:2101.04123 [cond-mat].
- [37] Wang, L. *et al.* Evidence for a fractional fractal quantum hall effect in graphene superlattices. *Science* **350**, 1231–1234 (2015).
- [38] DaSilva, A. M., Jung, J. & MacDonald, A. H. Fractional hofstadter states in graphene on hexagonal boron nitride. *Phys. Rev. Lett.* **117**, 036802 (2016).
- [39] Leconte, N., Javvaji, S., An, J. & Jung, J. Relaxation effects in twisted bilayer graphene: a multi-scale approach (2019). arXiv:1910.12805.
- [40] Gmitra, M. & Fabian, J. Graphene on transition-metal dichalcogenides: A platform for proximity spin-orbit physics and optospintronics. *Phys. Rev. B* **92**, 155403 (2015).
- [41] Li, Y. & Koshino, M. Twist-angle dependence of the proximity spin-orbit coupling in graphene on transition-metal dichalcogenides. *Phys. Rev. B* **99**, 075438 (2019).
- [42] Shin, J., Park, Y., Chittari, B. L., Sun, J.-H. & Jung, J. Electron-hole asymmetry and band gaps of commensurate double moire patterns in twisted bilayer graphene on hexagonal boron nitride. *Phys. Rev. B* **103**, 075423 (2021).
- [43] Xie, Y. *et al.* Fractional Chern insulators in magic-angle twisted bilayer graphene (2021). arXiv:2107.10854 [cond-mat].
- [44] Fast parallel algorithms for short-range molecular dynamics. *Journal of Computational Physics* **117**, 1–19 (1995).
- [45] Leconte, N., Jung, J., Lebègue, S. & Gould, T. Moiré-pattern interlayer potentials in van der waals materials in the random-phase approximation. *Phys. Rev. B* **96**, 195431 (2017).
- [46] Lehoucq, R. B., Sorensen, D. C. & Yang, C. Solution of large scale eigenvalue problems by implicitly restarted arnoldi methods. *ARPACK USERS GUIDE* .
- [47] Jung, J. & MacDonald, A. H. Tight-binding model for graphene pi-bands from maximally localized wannier functions. *Phys. Rev. B* **87**, 195450 (2013).
- [48] Trambly de Laissardière, G., Mayou, D. & Magaud, L. Numerical studies of confined states in rotated bilayers of graphene. *Phys. Rev. B* **86**, 125413 (2012).

- [49] Moon, P. & Koshino, M. Energy spectrum and quantum hall effect in twisted bilayer graphene. *Phys. Rev. B* **85**, 195458 (2012).

SUPPLEMENTARY INFORMATION

I. SIMULATION

Here, we outline the details of the tight-binding hopping terms, in particular the interlayer coupling that we have used in our simulations. We then show the band structures corresponding to a shifted origin 1D potential that shows the relative robustness of band folding features. We further present band structures for different Hamiltonian model parameters without and with spin-orbit coupling (SOC) terms to better understand the role of the different terms in the Hamiltonian.

A. Twisted bilayer graphene's tight-binding Hamiltonian

The twisted bilayer graphene (TBG) interlayer hopping terms between atoms at lattice points \mathbf{R}_i and \mathbf{R}_j are given by [39]

$$-t_{lm} = -t(\mathbf{R}_l, \mathbf{R}_m) = S_0 \exp[(\mathbf{d} \cdot \mathbf{e}_z - p)/q] \times \left[V_{pp\sigma}(d) \left(\frac{\mathbf{d} \cdot \mathbf{e}_z}{d} \right)^2 \right]. \quad (3)$$

with $\mathbf{d} = \mathbf{R}_l - \mathbf{R}_m$, $d = |\mathbf{d}|$ and \mathbf{e}_z the unit vector parallel to the z axis and where [48]

$$V_{pp\sigma}(d) = V_{pp\sigma}^0 \exp\left(-\frac{(d - d_0)}{r_0}\right) \quad (4)$$

with d_0 the interlayer distance, a_0 the interatomic carbon distance, $r_0 = 0.184a$ and $V_{pp\sigma}^0 = -0.48$ eV is the transfer integral between two vertically aligned atoms. This form in Eq. 4 is widely used in the literature [49] and is good at reproducing the largest magic angle in TBG, even though the corresponding effective hopping term, obtained by summing intralayer intra-sublattice terms [47], of -2.45 eV (when using $V_{pp\pi}^0 = 2.7$ eV for the transfer integral between nearest-neighbor atoms) corresponds to a Fermi velocity which is much smaller than experiment or even local density approximation (LDA). To correct for this approximate model in square brackets, we introduced the variables $p = 1.34$ and $q = 3.25$ to better capture the inter-layer distance modulations that enter the fitting procedure to the DFT tunneling at the K-point for all slidings as well as the magic angle renormalization factor S_0 equal to 0.895 for these structures that we relaxed using LAMMPS MD relaxations [44] using EXX-RPA-informed [45] force fields. This choice of S_0 value leads to the maximum flatness of bands at 1.08° when all terms but the first are equal to zero in the Hamiltonian from Eq. (2) in the manuscript. For the intralayer terms we simply use the F2G2 model [47].

B. Doubling of the bands due to band-folding

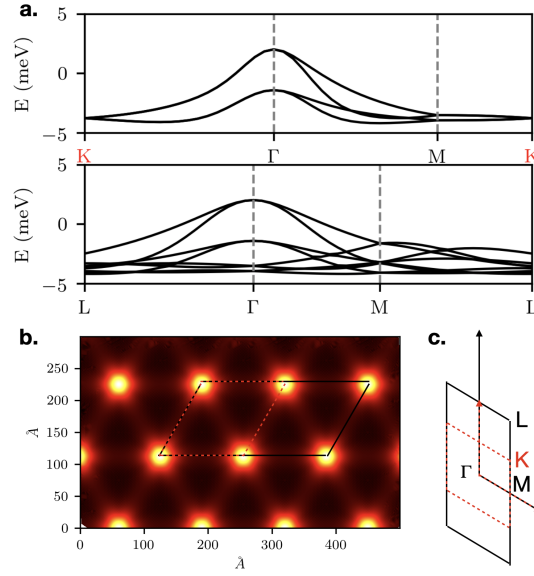
In Fig. S1, we illustrate how the existence of a potential that doubles the initial TBG moiré period by a factor two effectively leads to band-folding and associated doubling of the initial 4-fold degenerate valence and conduction bands. We calculate the band structures in the smallest moiré triangular unit cell and compare with the folded bands with twice the original unit cell area where we can observe how the initial bands are being doubled in number. We neglect any spin/valley degeneracy lifting terms in the Hamiltonian and will discuss their effect further in Sect. ID.

C. Alternative 1D potential modulation

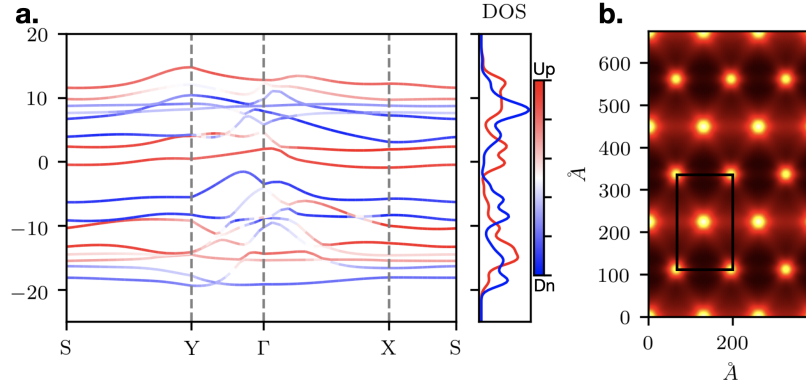
We have chosen a specific form of the 1D sine potentials in the main text to obtain the folded bands in the larger period cell. Here, we provide an additional 1D potential that leads to a doubled supercell area compared to the moiré pattern unit cell area that leads to quantitatively different types of folded bands. In Fig. S2, we apply a cosine instead of a sine 1D modulation in Eq. 2 in the manuscript (set $\phi = \pi/2$). In this case, the AA stacking regions are located where the 1D potential is maximal or minimal.

D. Role of the different Hamiltonian terms

In Figs. S3, S4, and S5, we revisit the band-structure shown in the manuscript main text consisting of a rectangular unit cell and sine 1D modulation potential to illustrate the effect of the different terms in our Hamiltonian in more

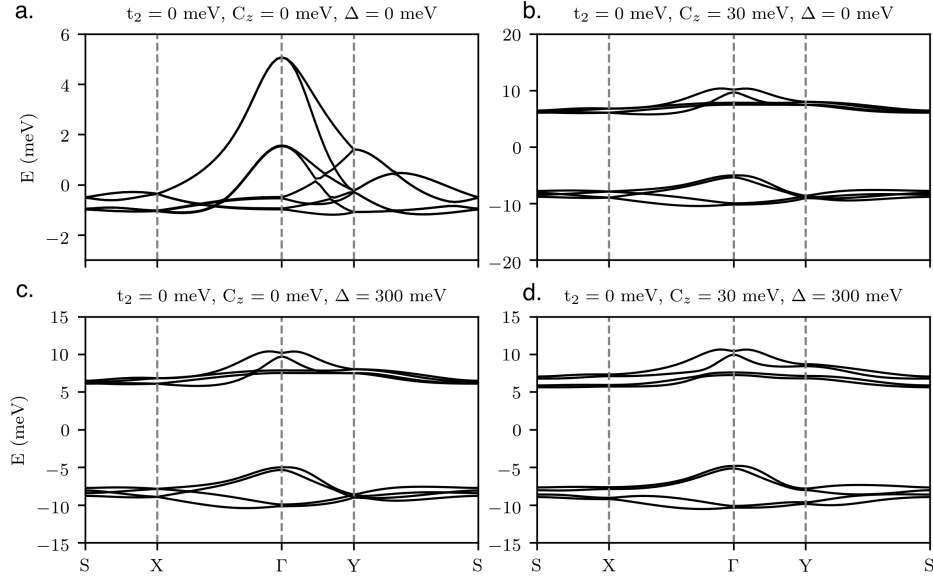


Supplementary Fig. S1. Band folding and doubling of bands. **a.** The top panel illustrates the bandstructure for the unperturbed original triangular moiré cell illustrated by the parallelogram linking 4 closest AA-stacking bright dots in **b.**, whereas the bottom panel shows the band structure for the doubled area supercell. The spin is neglected in this figure, as such we see a total of 4 bands (two valleys for the conduction band and valence band) in the top panel becoming 8 bands by band-folding in the bottom panel. **b.** Real-space schematic of the single and double area supercells indicated by the dashed red and black solid parallelograms. **c.** The associated BZ for the band structures for the single and double area supercells indicated also with dashed red and black solid lines.

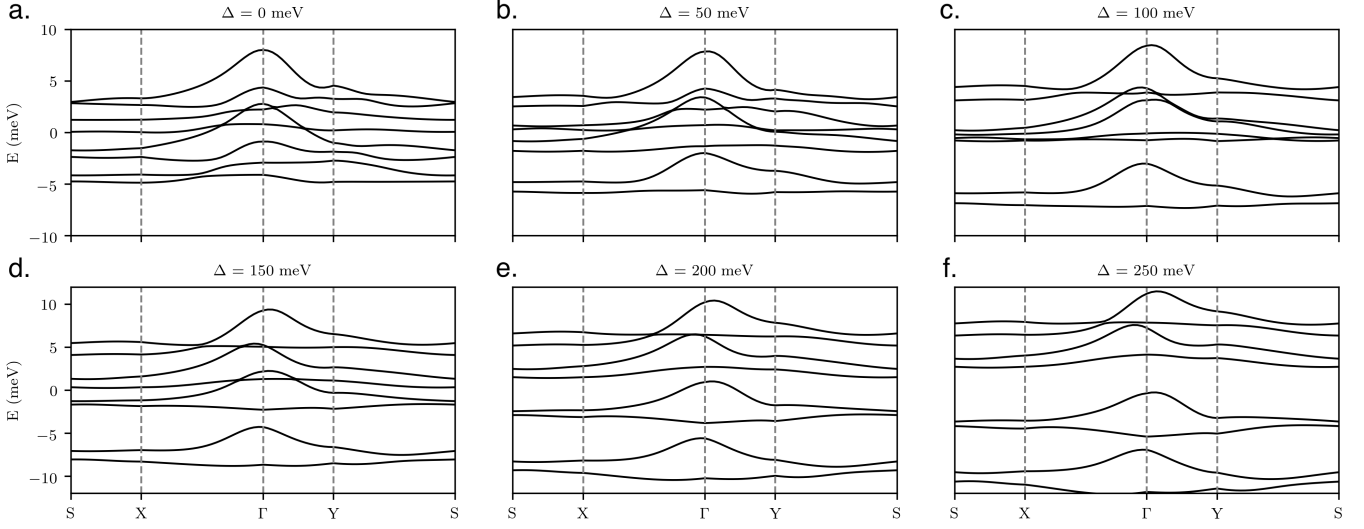


Supplementary Fig. S2. Cosine modulation for 1D potential in the rectangular unit cell. **a.** Bandstructure of TBG under a 1D cosine periodic potential in Eq. 2 by setting $\phi = \pi/2$, and using the same parameters $C_z = 30$ meV, $t_2 = 15$ meV, $\lambda_R = 10.5$ meV and $\Delta = 300$ meV. **b.** Colormap illustrating the cosine modulation in the rectangular unit cell using the same procedure as in the main text. The high-symmetry path in the Brillouin zone (BZ) is the same as in the manuscript.

detail. In Fig. S3, we divide in different panels the band structures and start by showing in Fig. S3a the band structure for the TBG, nearly flat bands in the rectangular unit cell. The area of this rectangular unit cell is twice as large as the area of the single TBG system (smallest parallelogram delimited by 4 AA-stacking regions); hence we observe a doubling in the number of the flat bands. In the absence of spin, but including the valley degeneracy (inherent to our real-space approach), we have 8 flat bands in the system, distributed evenly among conduction and valence bands. In Fig. S3b, we include the 1D sine modulation pattern and observe a clear energy separation of the conduction and valence bands. Alternatively, in Fig. S3c, we check the effect of adding a constant mass-term in the bottom graphene layer using the rectangular unit cell in the absence of a sine modulation. We see that in this case, the conduction bands and valence bands are being separated from each other too, but for our choice for the value of Δ , the doubled conduction bands remain very close to each other and cannot be disentangled at the meV energy level (same observation for the doubled valence bands). We finally combine in Fig. S3d the effect of both the sine potential and the constant mass-term. The 4 valence and 4 conduction bands get separated into 2 sets of 2 bands each. We note that the weak band degeneracy lifting at the high symmetry points originates in the ξ_{c_i} factor, which differentiates between sublattices that we have included in our 1D sine modulation. We have checked that in the absence of this

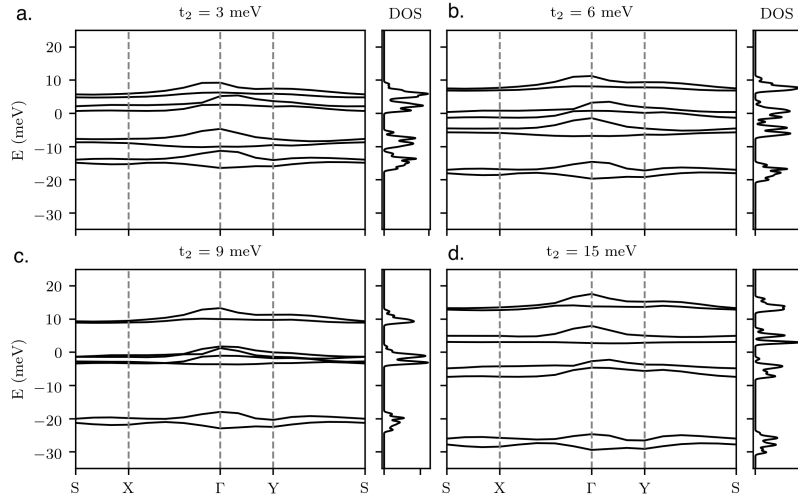


Supplementary Fig. S3. Impact of the different Hamiltonian terms. We gradually include the different terms from the Hamiltonian in Eq. 2 from the manuscript, while ignoring the Kane-Mele term by setting $t_2 = 0$ as well as the Rashba term by setting $\lambda_R = 0$ meV. Comparison of these figures with the final band structure in the manuscript illustrates that each term of this heuristic Hamiltonian can play an important role.



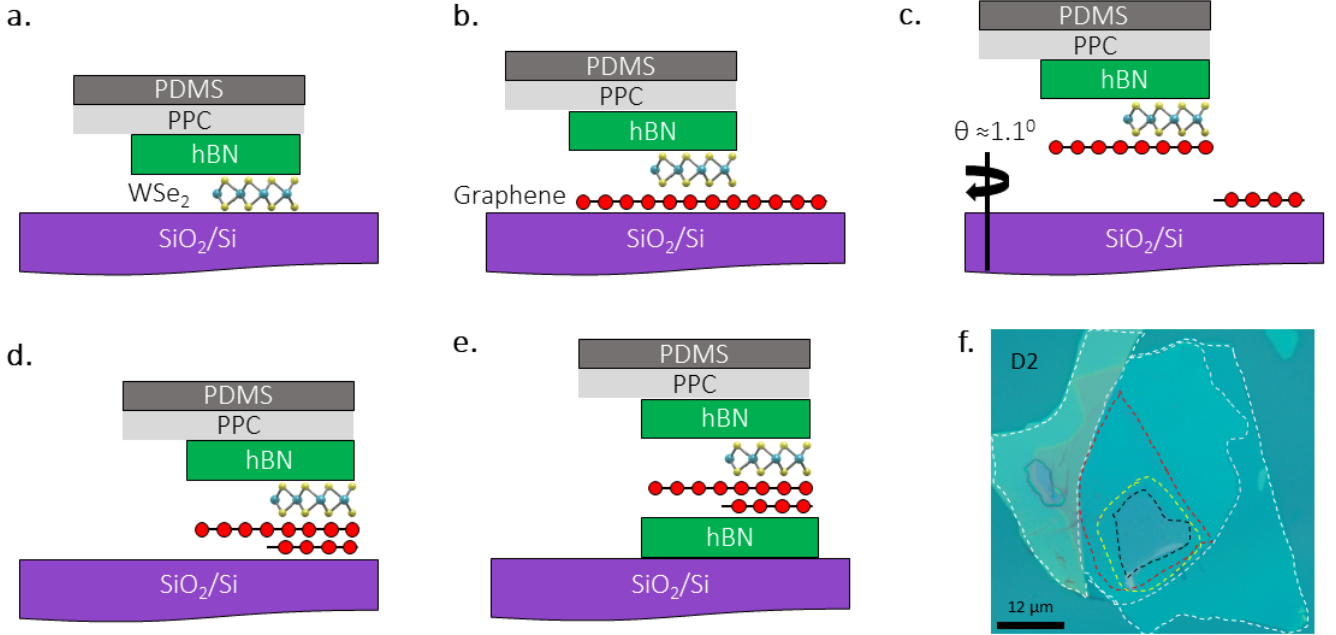
Supplementary Fig. S4. Effect of the constant mass-term in the band separation. We gradually increase the constant mass-term, with $t_2 = 3$ meV and $\lambda_R = 0$ meV, we only show the spin up contribution here, and $C_z = 0.03$ meV in Eq. 2 from manuscript. The constant mass term clearly increases the separation between the conduction and valence band groups that is expected to reduce interband screening and therefore enhance the chances of opening a band gap due to Coulomb interactions when the subbands are completely filled.

factor, this degeneracy lifting is nonexistent. Finally, for the case in Fig. S3d, only the Rashba and the Kane-Mele term are missing when compared to the band structure from the paper; this shows that for this choice of parameters, these terms are crucial in their ability to resolve the degeneracy lifted spins that are causing the features at $\nu = 0.5$ and 3.5 . In Fig. S4, we further discuss qualitatively the effect of either the mass-term in the presence of a constant Kane-Mele term, and in Fig. S5, we vary the magnitude of the Kane-Mele term that can arise due to proximity effects induced by the substrate. We omit the Rashba term for simplicity here and only show the spin-up component. We notice that while the mass-term tends to push the highest set of valence bands above the lowest set of the conduction band, the Kane-Mele term shifts them in the opposite directions. The combination of these two terms recovers the original ordering of the bands, and both terms tend to widen the energy spectrum range where the nearly flat bands distribute.

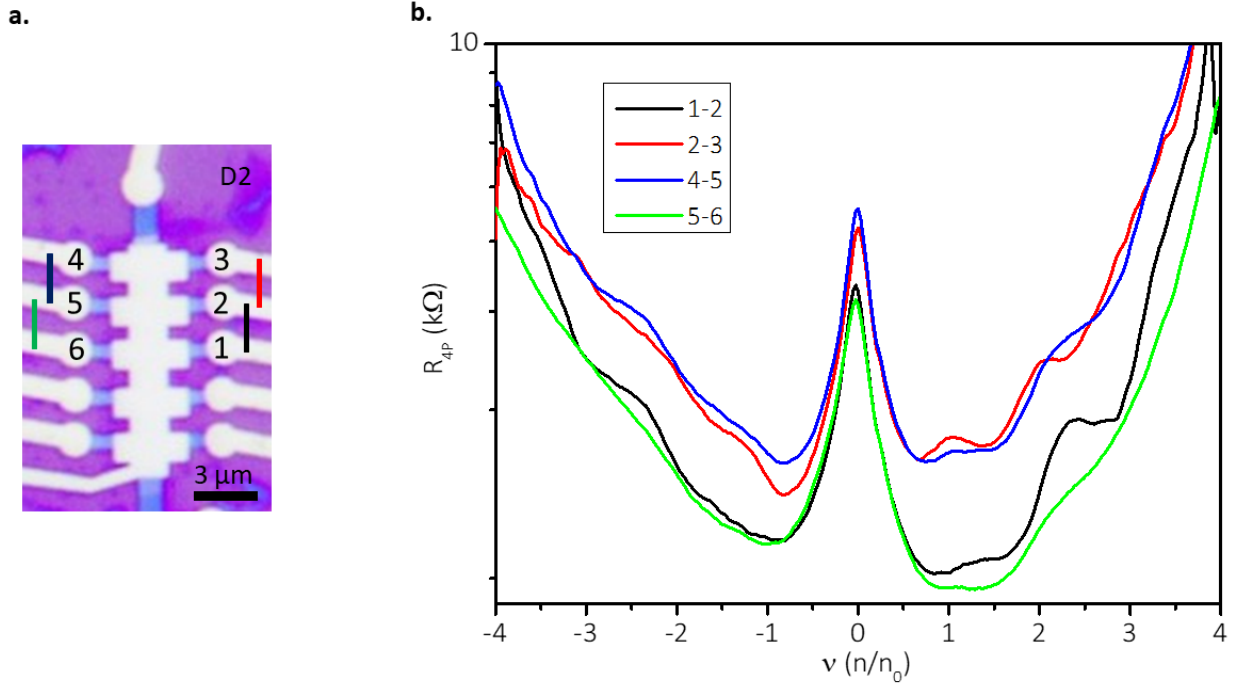


Supplementary Fig. S5. Effect of the the value of t_2 controlling the strength of the Kane-Mele term. We gradually increase the value of the Haldane pre-factor t_2 entering the Kane-Mele term, with $C_z = 30$ eV, $\Delta = 300$ meV and $\lambda_R = 0$ eV, in Eq. 2 from manuscript (we only show the spin-up component). Increasing the value of t_2 resolves the degeneracy of the spin-up and spin-down bands in momentum space although it does not lead to an overall splitting in the DOS.

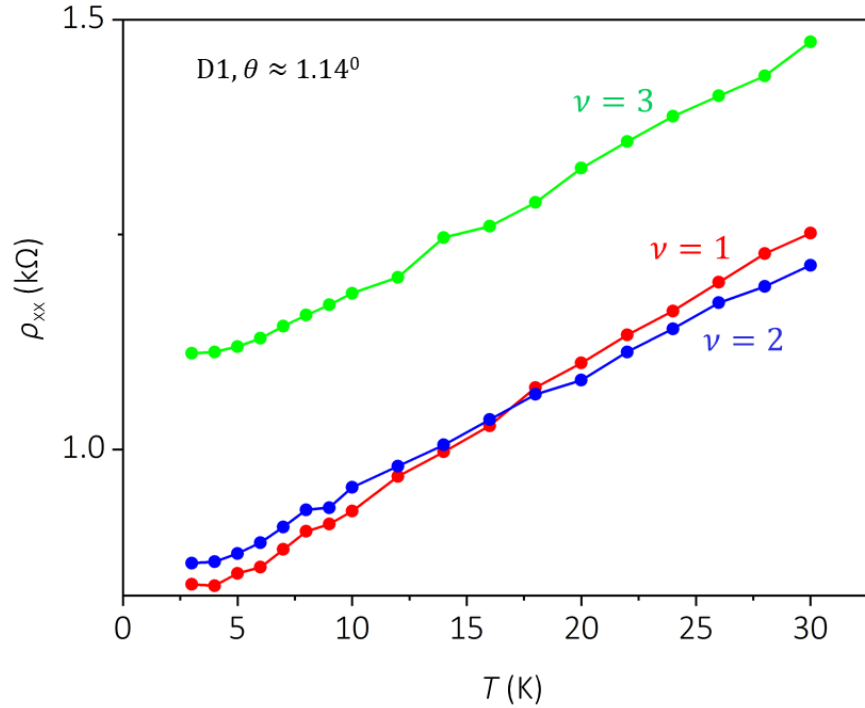
II. EXPERIMENTAL RESULTS



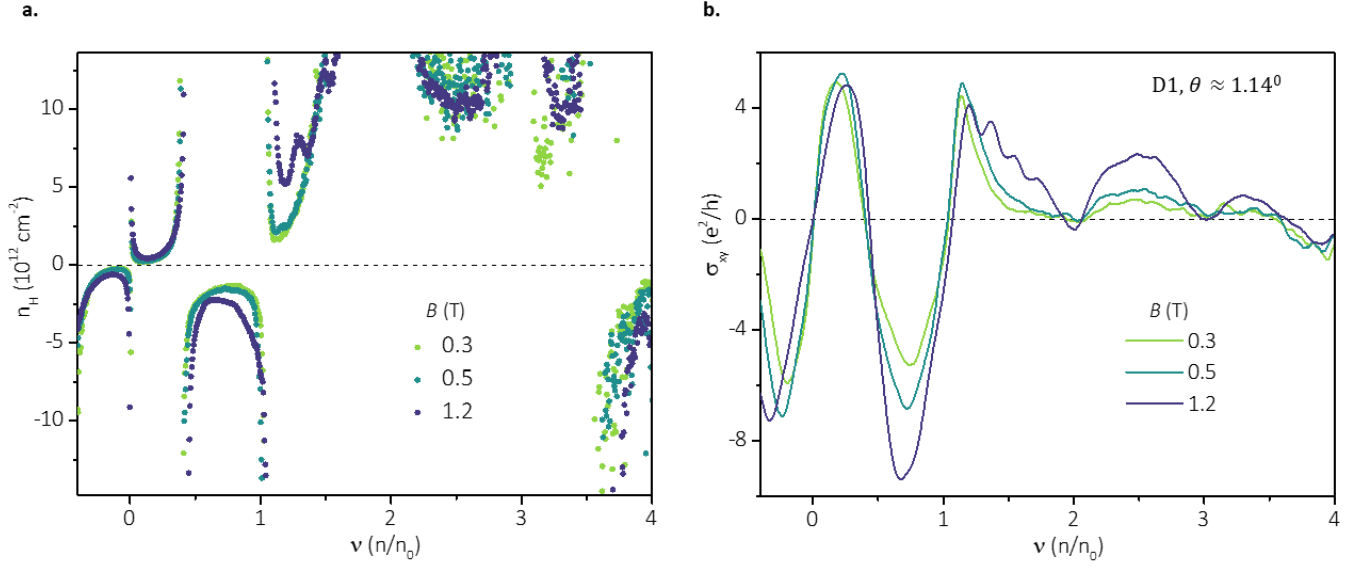
Supplementary Fig. S6. Device fabrication. **a-e.** Schematic of the various steps in the ‘tear and stack’ method used for fabrication of the moiré heterostructure. A layer of PDMS/PPC on a glass slide is used to sequentially pick the various heterostructure layers. A twist angle of $\approx 1.1^\circ$ is used to create the magic-angle twisted bilayer graphene. **f.** Optical image of the final stack for device D2. The top and bottom graphene (red and yellow), WSe_2 (black) and two hBN (white) layers are shown using dashed lines. The scale bar is $12 \mu\text{m}$.



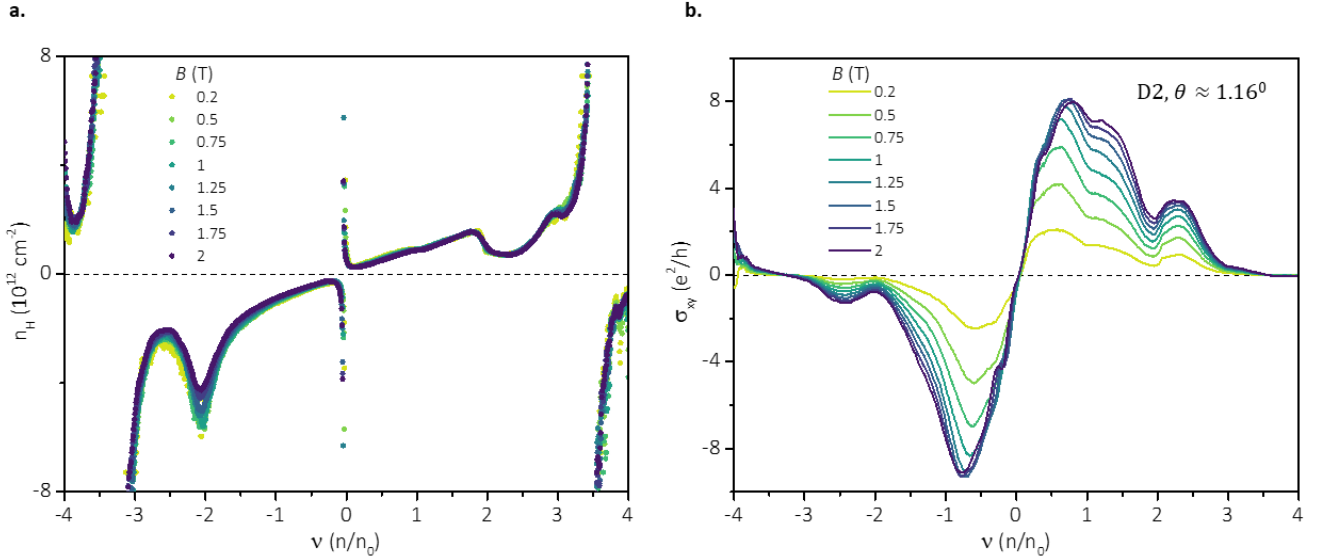
Supplementary Fig. S7. Characterization of device D2. **a.** Optical image of device D2 where the scalebar denotes $3 \mu\text{m}$. **b.** Four-probe resistance measurements at $T = 6 \text{ K}$ for different pair of contacts show twist angle uniformity throughout the TBG/WSe₂ channel. Different colors have been used for different pairs of voltage probes. Cr/Au top gate (see (a)) was used to tune the carrier density in the Hallbar.



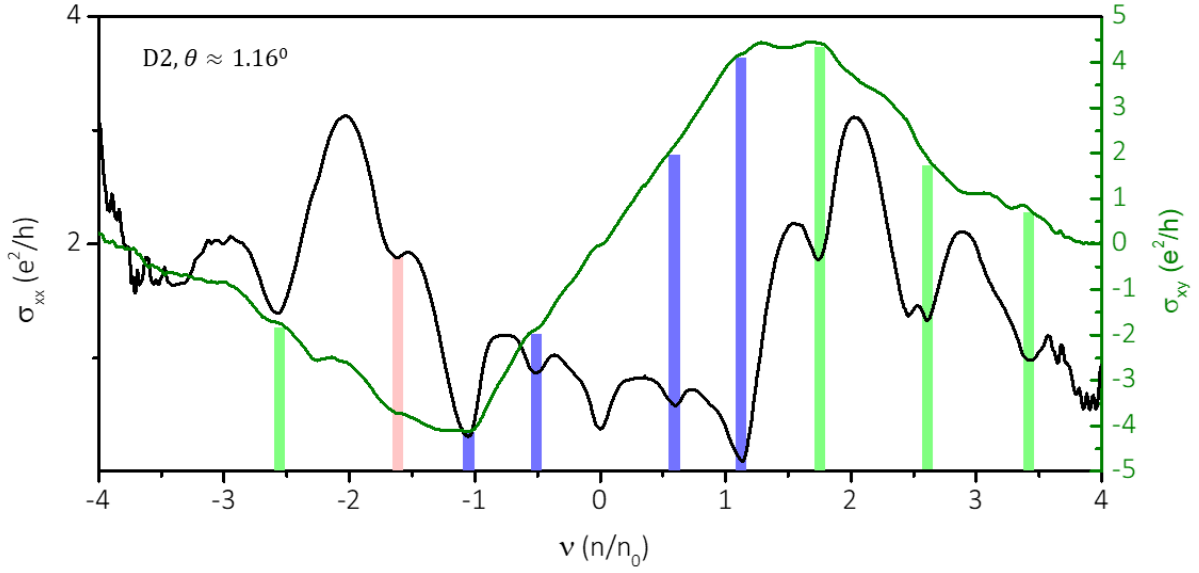
Supplementary Fig. S8. Linear-in- T resistance in device D1, $\theta \approx 1.14^\circ$ The longitudinal resistivity ρ_{xx} at various filling factors $\nu = 1, 2$ and 3 vary linearly with T in the measured range of temperature ($3 - 32 \text{ K}$). The slopes for $\nu = 1, 2$, and 3 were found to be $16, 13$, and $14 \Omega/\text{K}$ respectively.



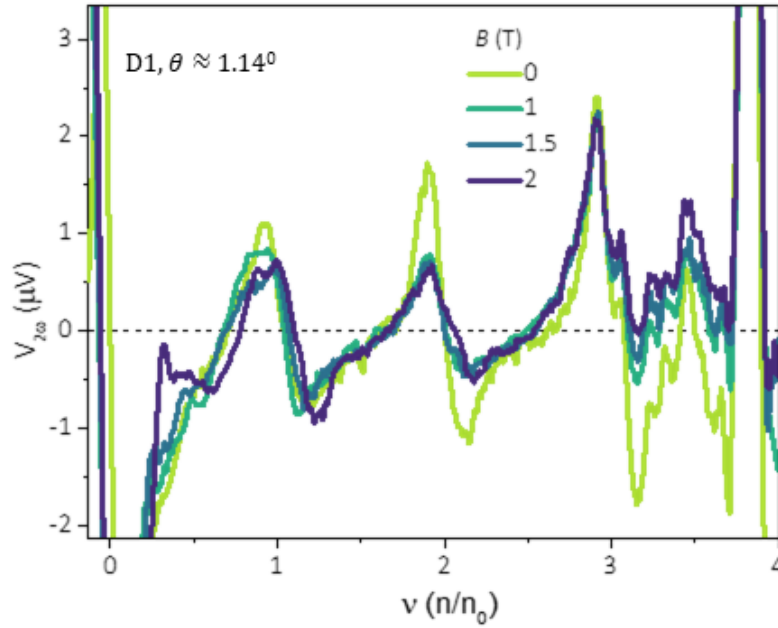
Supplementary Fig. S9. Low-field Hall data in device D1, $\theta \approx 1.14^\circ$. **a.** $n_H - \nu$ plot for $B = 0.3 - 1.2$ T. **b.** σ_{xy} as a function of ν for the same range of B . The zero crossings at $\nu = 0.5, 1$ and 3.5 and reset at $\nu = 2$ and 3 are robust with B .



Supplementary Fig. S10. Low field Hall data in device D2, $\theta \approx 1.16^\circ$. **a.** $n_H - \nu$ plot for $B = 0.2 - 2$ T. The sign-change at $\nu = 3.5$ appears at the lowest B -field of 0.2 T. In addition, the reset at charge carriers is observed at $\nu = \pm 2$. **b.** σ_{xy} as a function of ν for the same range of B .



Supplementary Fig. S11. Hall conductivity at $B = 9$ T in device D2. a. σ_{xy} shows plateaus as $\sigma_{xy} = Ce^2/h$ associated with the minima in σ_{xx} . Different color bars (blue for the CNP, green for $\nu = 1, \pm 2, 3$ and red for $\nu = -0.5$) have been used to show the sequence of symmetry-broken quantized states nucleating from several partial fillings of flat bands.



Supplementary Fig. S12. Magneto-thermoelectricity measurements in device D1. Thermoelectric voltage $V_{2\omega}$ measured at $B = 0, 1, 1.5,$ and 2 T and $T = 3$ K for a heating current of 300 nA. The feature at $\nu = 3.5$ is clearly visible at all B .